Journal of Zhejiang University-SCIENCE A (Applied Physics & Engineering)
ISSN 1673-565X (Print); ISSN 1862-1775 (Online)
www.jzus.zju.edu.cn; link.springer.com
E-mail: jzus_a@zju.edu.cn

Effects of the geometrical parameters of the injection nozzle on ethylene-air continuous rotating detonation*

Wei-jie FAN, Jin ZHOU†‡, Shi-jie LIU, Hao-yang PENG

Science and Technology on Scramjet Laboratory, College of Aerospace Science and Technology, National University of Defense Technology, Changsha 410073, China

†E-mail: zj706@vip.sina.com

Received July 17, 2020; Revision accepted Sept. 25, 2020; Crosschecked June 23, 2021

Abstract: Compared with traditional isobaric combustion, continuous rotating detonation (CRD) has been theoretically proved to be a more efficient combustion mode with higher thermal cycle efficiency. However, the realization and stable operating of liquid kerosene detonation is still a challenge. As a major component of kerosene pyrolysis products after regenerative cooling, ethylene is a transitional hydrocarbon fuel from kerosene to hydrogen and it is worth studying. In this paper, a series of 2D numerical simulations are conducted to investigate the effects of the injection nozzle on the ethylene-air CRD. Three geometrical parameters of the nozzle are thoroughly tested including the distance between two neighboring nozzle centers, the nozzle exit width, and the slant angle of the nozzle. The results show that an ethylene-air detonation wave is realized and it propagates stably. A small distance between two neighboring nozzle centers is conducive to improving the strength of the CRD wave and leads to greater feedback pressure into the plenum. As the nozzle exit width increases, the strength of the CRD wave and the feedback pressure into the plenum both increase. The CRD wave propagation velocity is greatly improved and the feedback pressure into the plenum is significantly reduced when the slant angle of the nozzle is positive. By contrast, a sizeable reduction in velocity is found when the angle is negative. The co-rotating two-wave propagation mode is observed when the angle is 30°, and the highest CRD propagation velocity and the lowest feedback pressure are both obtained when the angle is 60°.

Key words: Continuous rotating detonation (CRD); Ethylene-air; Injection nozzle; Feedback pressure
https://doi.org/10.1631/jzus.A2000314 **CLC number:** V43

1 Introduction

Many aerospace propulsive systems work by isobaric combustion, including rocket engines, turbojet engines, ramjets, and scramjets (Wang and Shen, 2019; Huang et al., 2020; Shi et al., 2020; Sun et al., 2020). However, the propulsive performance of isobaric combustion has almost reached its upper theoretical level. Compared with isobaric combustion, detonation is a promising combustion form that may achieve better propulsion performance due to its higher thermodynamic efficiency and quicker heat release rate (Bykovskii and Vedernikov, 1996; Stewart and Kasimov, 2006; Lei et al., 2020a, 2020b). Generally, a detonation engine can be classified as a pulse detonation engine (PDE) (Nikitin et al., 2009), an oblique detonation engine (ODE) (Cai et al., 2016) or a continuous rotating detonation engine (CRDE) (Lin et al., 2015; Anand et al., 2016a, 2016b). A schematic of the conventional CRDE is shown in Fig. 1 (Yao et al., 2017). Fuel and oxidizer are injected at the head of the annular combustion chamber and the continuous rotating detonation (CRD) wave propagates circumferentially consuming the combustible propellant. Then the combustion products exhaust at the other end of the chamber with high velocity and pressure producing a

‡ Corresponding author
* Project supported by the National Natural Science Foundation of China (Nos. 51776220 and 91541103) and the Postgraduate Scientific Research Innovation Project of Hunan Province, China
ORCID: Wei-jie FAN, https://orcid.org/0000-0002-4766-5494; Jin ZHOU, https://orcid.org/0000-0002-0563-4411

stable thrust. CRDE can operate over a wide range of flight Mach numbers. Additionally, CRDE does not require repeated ignition and it works continuously with a high frequency once initiated. Therefore, it attracts great attention in the propulsive research field and is studied extensively (Zhdan, 2008; Hishida et al., 2009; Nordeen et al., 2016; Gaillard et al., 2017; Sun et al., 2017, 2018a, 2018b).

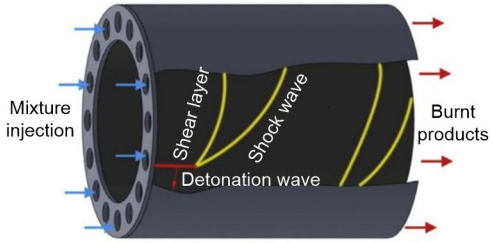

Fig. 1 Schematic of a typical CRDE. Reprinted from (Yao et al., 2017), Copyright 2016, with permission from Springer Nature

Voitsekhovskii (1959) proposed the concept of stationary detonation and realized C_2H_2-O_2 CRD in a disk-shaped experimental device. Nicholls et al. (1966) realized a short CRD wave in an annular combustion chamber and verified the feasibility of CRDE. In the past decades, the working processes of CRDE have been extensively studied, including initiation, propagation characteristics, and propulsive performance. Numerical simulations utilizing premixed gas and the ideal injection model have been carried out to reveal the structure of the basic CRD wave flow field. Taki and Fujiwara (1978) two-dimensionally simulated premixed hydrogen-oxygen detonation using a two-step reaction model. Their numerical results agreed with experimental observations under the same conditions. Zhdan et al. (1990, 2007) numerically studied the hydrogen-oxygen CRD wave and obtained its flow field structure. Davidenko et al. (2007) used a detailed chemical mechanism and a high-order shock-capturing scheme to simulate the CRD of a stoichiometric hydrogen-oxygen mixture. The flow field structure was obtained and was consistent with that in the experiment.

Many simulations use the ideal injection model and neglect the process of propellant injection. However, that process has great effects on the propagation of the CRD wave. The ideal injection model assumes that the premixed gas is injected through a number of micro-nozzles which are uniformly distributed at the inlet of the combustion chamber. However, in order to avoid flashback, fuel and oxidizer are usually injected into the chamber separately through discrete injectors and a slot (Li et al., 2018; Wang et al., 2018; Xie et al., 2018), and thus the process of propellant injection is hard to simulate by using an ideal injection model. Great efforts to reveal that process have been made in the CRD field. Anand et al. (2015) conducted non-premixed experiments using different fuel injection orifice sizes and air injection gap widths. A low frequency pulsation of the CRD wave was found during CRDE operation and the results indicated that pulsation of the wave was linked to the injection sizing and the fuel plenum pressure. In a further study, Anand et al. (2016a) experimentally analyzed the feedback pressure of the CRD wave in the air injection gap and the propellant plenum. The fundamental frequency of the air injection gap's pressure oscillation was consistent with that of the CRD wave, while the low frequency oscillation in the plenum stayed constant. However, Naples et al. (2015) found the frequency oscillation in the fuel injector was not in line with that of the CRD wave. Rankin et al. (2015) experimentally studied the impacts of the air inlet slot width on the static pressure in the plenum. The results showed that the amplitude of high frequency pressure oscillation in the plenums increased as the width of the slot was increased, and the interference to the air plenum became more obvious. Schwer and Kailasanath (2012) numerically analyzed the feedback pressure into the propellant plenum by using three kinds of injector: slot, cylindrical, and pintel micro-injectors. Results indicated the feedback pressure could be significant and reach up to 77% of the plenum stagnation pressure. Further numerical study on reducing feedback pressure was carried out (Schwer et al., 2013). When the nozzle was slanted towards the incoming CRD wave, the pressure oscillation in the propellant plenum was enhanced. The maximum slant angle was 40° and no efficient way to reduce the feedback pressure was proposed in the study. The mechanism of reducing feedback pressure needs further study. Sun et al. (2017) studied the effects of injection nozzle exit width on the hydrogen-air CRD wave using 2D simulations. The transition of the CRD wave propagation mode and pressure oscillation in the plenum were observed. Three-dimensional simulations under non-premixed conditions were also carried out

(Frolov et al., 2013; Liu M et al., 2015; Nordeen et al., 2016; Smirnov et al., 2018). When the total mass flow rate increased, a two-wave propagation mode was observed (Sun et al., 2018a). The two-wave propagation mode was more likely to form in the CRDE with a small air throat width (Sun et al., 2019).

In recent years, hydrocarbon detonation has aroused great interest in many researchers because a hydrocarbon fuel is considered a more reliable and affordable option for engineering applications compared with hydrogen. Experiments have been carried out to determine the operating range and propagation characteristics of hydrocarbon detonation in the cases of methane, ethane, ethylene, and propane (Kindracki et al., 2011; Huang et al., 2019; Peng et al., 2019a, 2019b; Liu et al., 2020). Although hydrocarbon detonation was successfully initiated and was deemed feasible, great velocity reduction was observed. Due to the low chemical activity of liquid kerosene, achieving stable propagation of liquid kerosene detonation is still challenging. As a major component of kerosene pyrolysis products, ethylene is a transitional hydrocarbon fuel from kerosene to hydrogen, and ethylene detonation is worth studying. To get more detailed information about ethylene detonation, a few numerical simulations have been conducted (Schwer and Kailasanath, 2013; Fujii et al., 2016). It was found that the propagation velocity deficit and incomplete combustion were caused by insufficient mixing (Fujii et al., 2016). The basic flow field patterns and behaviors of ethylene CRD were compared with those of the hydrogen CRD (Schwer and Kailasanath, 2013). However, the effects of real nozzle injectors and propellant plenum were not taken into consideration in these 2D studies. Simulations on hydrocarbon CRD wave using a more realistic physical model are needed.

Due to CRD wave propagation, the flow in the CRDE has a strong circumferential aspect. In addition, there is generally little difference radically with the flow in the annular combustion chamber whose radical dimension is typically smaller than its azimuthal and axial dimensions (Schwer and Kailasanath, 2011, 2013). In consequence, the combustion chamber is usually "unrolled" into two dimensions, i.e. a rectangular chamber with periodic boundaries. In this study, 2D simulations on the ethylene-air CRD in the combustion chamber with real nozzle injectors and propellant plenum are carried out. Real injection nozzles and propellant plenum are added to the physical model to account for the transition of the CRD propagation mode. In addition, the feedback pressure in the plenum can be captured by using this physical model. A stoichiometric ethylene-air mixture is injected into the chamber through an array of rectangular nozzles. Effects of the nozzles' geometrical parameters on the CRD wave are analyzed with respect to the distance between two neighboring nozzle centers (W), the nozzle exit width (W_e), and the slant angle of the nozzle (α). The flow field and propagation characteristics of the CRD wave are obtained in different cases. The feedback pressure into the propellant plenum is also analyzed. The study enriches the understanding of the hydrocarbon CRD wave propagation characteristics and of the design theory of injection nozzles.

2 Physical model and numerical method

2.1 Physical model

The computational domain and nozzle geometry are shown in Fig. 2. A stoichiometric ethylene-air mixture is stored in the plenum and is injected into the combustion chamber through a uniformly distributed array of nozzles. The azimuthal length of the rectangular chamber is 300 mm except in the case where W=8 mm. In case W=8 mm, the azimuthal length of the chamber is 296 mm as the number of nozzles must be an integer. The axial length of the chamber is kept constant at 100 mm in all cases. The heights of the plenum and nozzle are 20 mm and 10 mm, respectively. To investigate the effects of the geometrical parameters of the nozzle on the CRD wave, the distance between two neighboring nozzle centers, W, varies as 6 mm, 8 mm, and 10 mm. The exit width of each nozzle, W_e, is also changed at 4 mm, 3 mm, and 2 mm. When the premixed gas is injected through the slanted nozzles, gas will run into the chamber with azimuthal velocity. That may have impacts on the propagation of the CRD wave. High pressure behind the CRD wave may not directly disturb the plenum due to the side walls of the slant nozzles. Thus, cases with slant injection nozzles are simulated. The slant angle of the nozzles, α, measured from the $+y$ direction, is set at 0°, ±30°, and ±60°. It is worth noting that

α is positive when the nozzles slant in the propagation direction of the CRD wave; otherwise, α is negative. When α is 0°, premixed gas is perpendicularly injected into the chamber. A variable-control is applied to the nozzle design, and the geometrical parameters of the different cases are listed in Table 1.

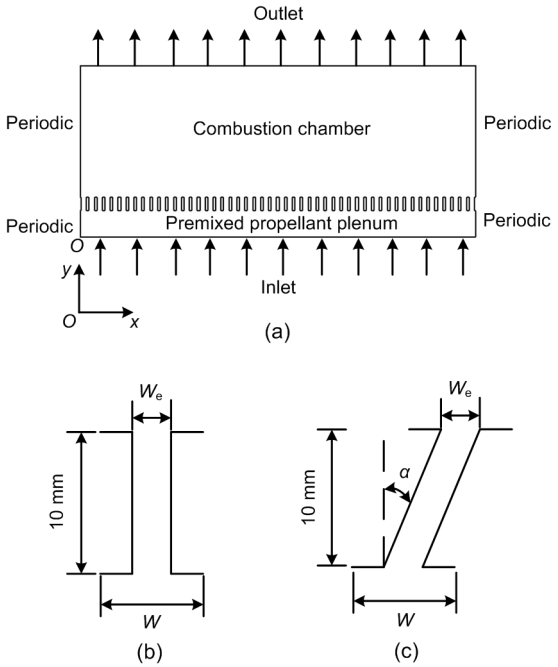

Fig. 2 Computation domain and nozzle geometry
(a) Whole computational domain; (b) Vertical injection nozzle; (c) Slant injection nozzle

Table 1 Geometrical parameters of the cases in this study

Case	W (mm)	W_e (mm)	α (°)
A0	6	4	0
A1	8	4	0
A2	10	4	0
B1	6	2	0
B2	6	3	0
C1	6	4	30
C2	6	4	−30
C3	6	4	60
C4	6	4	−60

2.2 Numerical method

All cases in this study are solved by ANSYS FLUENT which is widely used in research on the CRD wave (Driscoll et al., 2016; Sun et al., 2017, 2018a, 2018b; Meng et al., 2018). The propellant is a stoichiometric ethylene-air mixture and the ideal gas law is applied to calculate its density. Since the characteristic time scale of the chemical reaction is usually much shorter than that of the gas flow process in detonation simulations, the transport effects can be ignored. Therefore, the Euler equations are used to calculate the flow field in this study. These have been considered appropriate and have been adopted in much previous research (Shao et al., 2010; Liu et al., 2011; Sun et al., 2017). The explicit formulation of a density-based solver is used to solve the 2D Euler controlling equations. Physical fluxes are split by the Roe-averaged flux difference splitting (Roe-FDS) method, and gradients are solved by the least-square cell-based method. A second-order upwind scheme is employed to solve the flow equations and a second-order implicit scheme is applied for time stepping.

The chemical reaction is treated by a laminar finite rate reaction model and the reaction rate constants are determined by the Arrhenius formulation, i.e.

$$k_f = AT^b\left(\frac{-E_a}{RT}\right), \tag{1}$$

where k_f refers to the reaction rate constant, A is the pre-exponential factor, T is the temperature, R is the gas constant, E_a is the activation energy, and b is the temperature exponent. Details of the ethylene-air reaction model are listed in Table 2. The reduced kinetic model (Singh and Jachimowski, 1994; Morris, 2005) which treats 10 species and 10 elementary reactions is used, including N_2 as the 10th species. The collision efficiency and reverse reactions are accounted for to make the simulation more accurate. The reaction model was validated by comparing the computational results to those of the detailed kinetic model that had been validated against the experimental data (Singh and Jachimowski, 1994). In addition, Morris (2005) applied the reaction model to the pulse detonation and found the reaction model could generally do a good job of predicting the experimental data in the detonation tube. The model is therefore suitable for our study and the calculation results obtained by applying the model are reliable. In the calculation process, the chemical reaction only takes place in the combustion chamber. Similar restrictions are also applied in the open literature (Schwer and

Kailasanath, 2012; Sun et al., 2017). Moreover, two monitor points named P1 and P2 are placed in the plenum and chamber to record the pressure oscillations, and their corresponding coordinates are (120, 10) and (120, 35), respectively.

Table 2 Ten-step ethylene kinetic model

No.	Reaction*	A**	b	E_a (cal/mol)
1	$C_2H_4+O_2\rightleftharpoons CO+2H_2$	1.80×10^{14}	0.0	35500
2	$CO+OH\rightleftharpoons CO_2+H$	4.40×10^{6}	1.5	−740
3	$CO+O+M\rightleftharpoons CO_2+M$	5.30×10^{13}	0.0	−4540
4	$H_2+O_2\rightleftharpoons OH+OH$	1.70×10^{13}	0.0	48000
5	$H+O_2\rightleftharpoons OH+O$	2.60×10^{14}	0.0	16800
6	$OH+H_2\rightleftharpoons H_2O+H$	2.20×10^{13}	0.0	5150
7	$O+H_2\rightleftharpoons OH+H$	1.80×10^{10}	1.0	8900
8	$OH+OH\rightleftharpoons H_2O+O$	6.30×10^{16}	0.0	1090
9	$H+OH+M\rightleftharpoons H_2O+M$	2.20×10^{22}	−2.0	0
10	$H+H+M\rightleftharpoons H_2+M$	6.40×10^{17}	−1.0	0

* Third body efficiencies for all termolecular reactions: 2.5 for M=H_2, 16.0 for M=H_2O, and 1.0 for all other M. ** Units are in seconds, moles, cubic centimeters, calories, and degrees Kelvin

Pressure-inlet is applied for the inlet boundary, and the total pressure and total temperature are set constant as 500 kPa and 300 K, respectively. Pressure-outlet is applied at the exit of the chamber, where the environment pressure is set as 100 kPa. The left and right boundaries are periodic and they can exchange data to maintain the propagation of the CRD wave. A layer of combustible gas with a height of 5 mm is set at the head of the chamber before ignition. All the cases are then ignited by a 5 mm×5 mm tangential flow with high speed and high pressure in the preset flow field. The detail information of the preset flow field is shown in Fig. 3 and Table 3. As Fig. 4 shows, the pressure record curves of P1 in the plenum in Case B1 have little difference when it is calculated by shear-stress transport (SST) k-ω turbulence model with slip walls or Euler equations with non-slip walls. The averaged pressures in the plenum in Case B1 obtained by SST k-ω turbulence model with slip walls and Euler equations with non-slip walls are 497.45 kPa and 497.96 kPa correspondingly, which are in good agreement. Thus, all the walls are set as non-slip and adiabatic in this study.

The computational domain is meshed with hexahedral cells, and three scales of grid with average

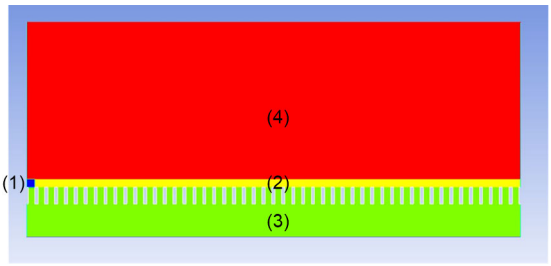

Fig. 3 Initial preset flow field
(1) Ignition area; (2) Combustible gas area; (3) Upstream flow area; (4) Downstream flow area

Table 3 Detailed information of the preset initial flow field

Area	P (kPa)	T (K)	u (m/s)	v (m/s)	Species
(1)	1000	300	1200/−1200	100	H_2O
(2)	100	300	0	100	Stoichiometric propellant
(3)	500	300	0	100	Stoichiometric propellant
(4)	100	300	0	300	Air

P is the pressure; u and v are the velocity components along the x-axis and y-axis, respectively

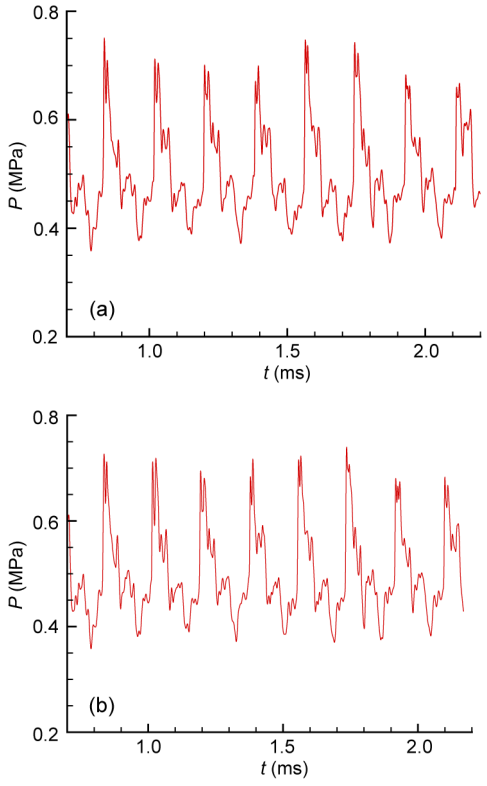

Fig. 4 Pressure record curves of P1 in the plenum in Case B1 with time t: (a) SST k-ω turbulence model with slip walls; (b) Euler equations with non-slip walls

sizes of 0.125 mm (fine), 0.25 mm (moderate), and 0.50 mm (coarse) are used to validate the grid independence. Fig. 5 shows the temperature contours of three grids, and the pressure trace curves recorded by monitor P2 of three different grids are plotted in Fig. 6. As the results show, similar flow field structures can be captured by three different grids. The pressure trace curves indicate that different grids are all able to give similar results. However, the interface between the fresh premixed gas and the detonation products is relatively smoother and a more detailed structure is indistinct in the case with coarse mesh. A moderate level of grid is applied in this study in consideration of both calculation accuracy and efficiency. The total number of cells used in this study is about 0.61 million in all cases. The physical time and number of time steps are 3 ms and 30000, respectively. All the cases in this study are run for more than 10 cycles to ensure that the detonation wave reaches a steady state. Additionally, the accumulation error is proportional to the number of time steps when solving transient processes, as discussed in detail by Smirnov et al. (2015). According to Smirnov et al. (2015), the reliability of the computational results can be determined by the following equations:

$$S_{\mathrm{err}}=\left(\frac{1}{N_x}\right)^{k+1}+\left(\frac{1}{N_y}\right)^{k+1}, \tag{2}$$

$$n_{\max}=\left(\frac{S^{\max}}{S_{\mathrm{err}}}\right)^2, \tag{3}$$

$$R_{\mathrm{s}}=\frac{n_{\max}}{n}, \tag{4}$$

where S_{err} is the total accumulated error. N_x and N_y are the number of cells in the x and y directions, and they are 1200 and 520 in this study, respectively. k is the order of accuracy of the numerical scheme and it is 2 in this study. $n_{\max}$ is the maximum allowable number of time steps. $S^{\max}$ is the allowable value of the total error which is presumed as 1%. n is the number of time steps and is 30000 in this study. The reliability of the results, R_{s}, can be calculated as 5.64×10^7 by using the above equations. The higher the value of R_{s}, the more reliable are the results. Since all the cases can achieve reliabilities higher than 10^7, the results in this study are credible.

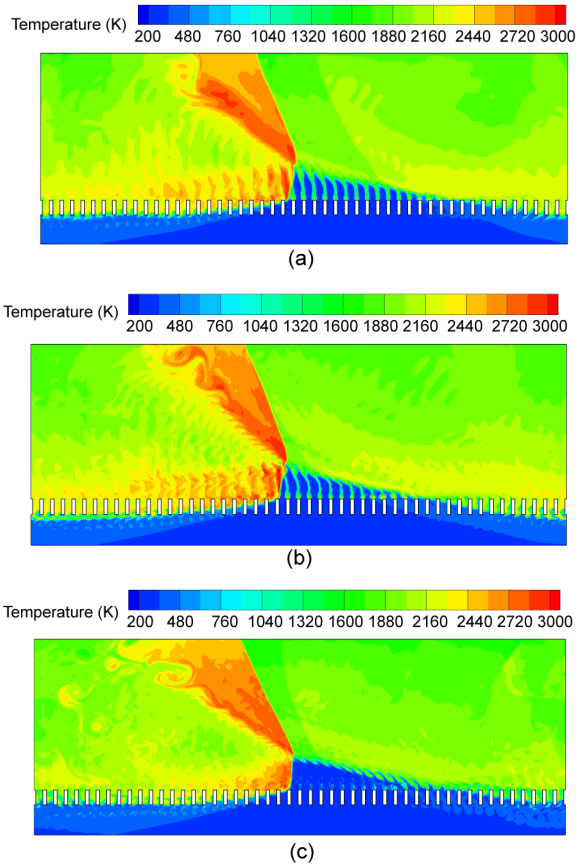

Fig. 5 Temperature contours of three different grid sizes at the time of t=0.6 ms
(a) Coarse; (b) Moderate; (c) Fine

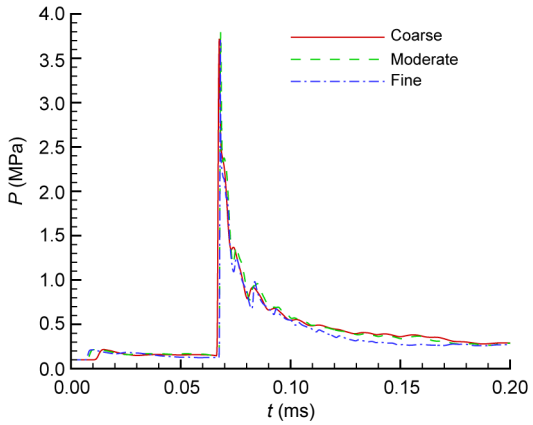

Fig. 6 Pressure curves of three different grid sizes recorded by P2

3 Results and discussion

All cases with different geometrical parameters in this study are summarized in Table 1 and Case A0

is used as the baseline geometry. In order to assess the effects of the injection nozzle, the flow field, propagation characteristics, and pressure oscillation in the plenum have been summarized and analyzed.

3.1 Effects of the distance between two neighboring nozzle centers

In this section, Cases A0–A2 with different W of 6 mm, 8 mm, and 10 mm are analyzed. As shown in Fig. 7, the flow fields of the three cases are basically similar, and consist of the CRD wave, oblique shock, the combustible gas layer in the shape of triangle in front of the CRD wave, current combustion products behind the CRD wave, and previous combustion products. Moreover, the CRD waves in the three cases all propagate in single-wave mode during the whole operating time. However, the CRD wave of Case A0 is much higher due to more injection nozzles in that case. As the gaps exist between injectors, the high-temperature products of the previous cycle of combustion cannot be totally blown downstream, and in turn heat the fresh premixed gas and generate high-temperature strips in the fill region. As W increases, the gaps between adjacent nozzles become wider and more premixed gas gets burned before the arrival of the CRD wave.

Fig. 8 shows the pressure trace curves recorded by monitor P2 in the chamber. When the CRD wave reaches P2 in the chamber, the high pressure of the CRD wave will be captured and the pressure curve will present a peak. The time interval that the CRD wave takes to propagate in a cycle can be calculated by the presence of peak pressures. Since the length of the chamber is known, the instantaneous propagation frequency and the instantaneous propagation velocity (V_d) of the CRD wave can be calculated. The average CRD wave propagation velocities ($\bar{V}_d$) of Cases A0–A2 are estimated as 1707.09 m/s, 1690.45 m/s, and 1657.38 m/s, indicating that $\bar{V}_d$ decreases slightly with the increase of W. Moreover, some peak pressures in the chamber in Case A0 can even exceed 2.5 MPa and they are much higher than those of Cases A1 and A2, which are generally lower than 1.5 MPa. These results all indicate that a stronger CRD wave with higher pressure in the chamber is obtained when W is smaller. In addition, some fluctuations of peak pressures in the chamber of each case are observed meaning that the strength of the CRD wave varies with time. That is mainly attributed to the interaction between CRD wave propagation and propellant injection. High pressure behind the CRD wave blocks the injection of premixed gas. A stronger CRD wave with higher pressure may lead to a longer block time. Thus, the height of the combustible gas layer decreases in the next cycle which in turn weakens the strength of the CRD wave. This is a spontaneous adjustment during the process of CRD wave propagation. We can see the peak pressures go up and down, which is called waxing and waning (Liu YS et al., 2015). Meanwhile, the fluctuation is much more obvious in Case A0, which indicates that the interaction between the propellant injection and CRD wave propagation is more pronounced when W is smaller.

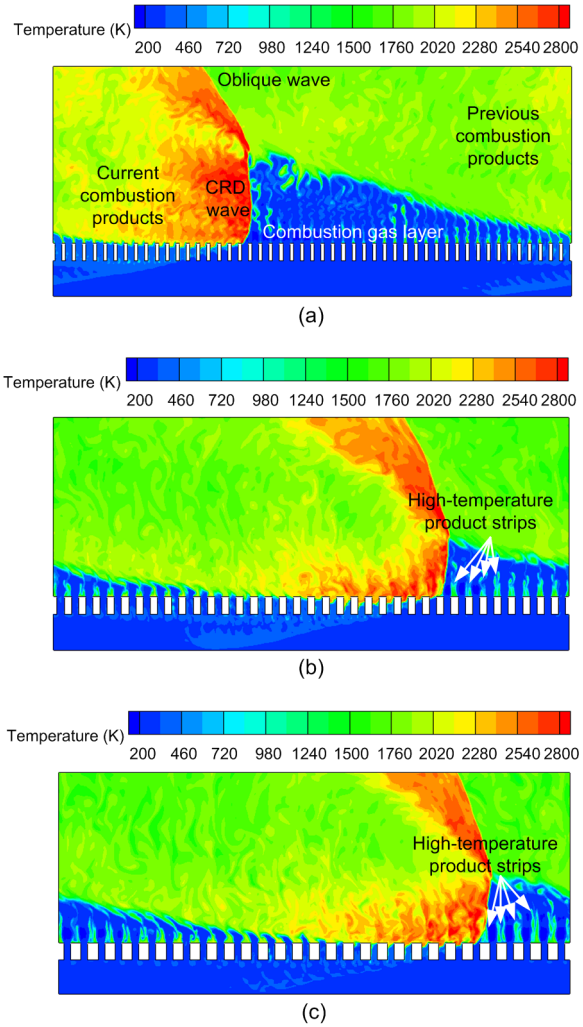

Fig. 7 Temperature contours of Cases A0–A2
(a) Case A0; (b) Case A1; (c) Case A2

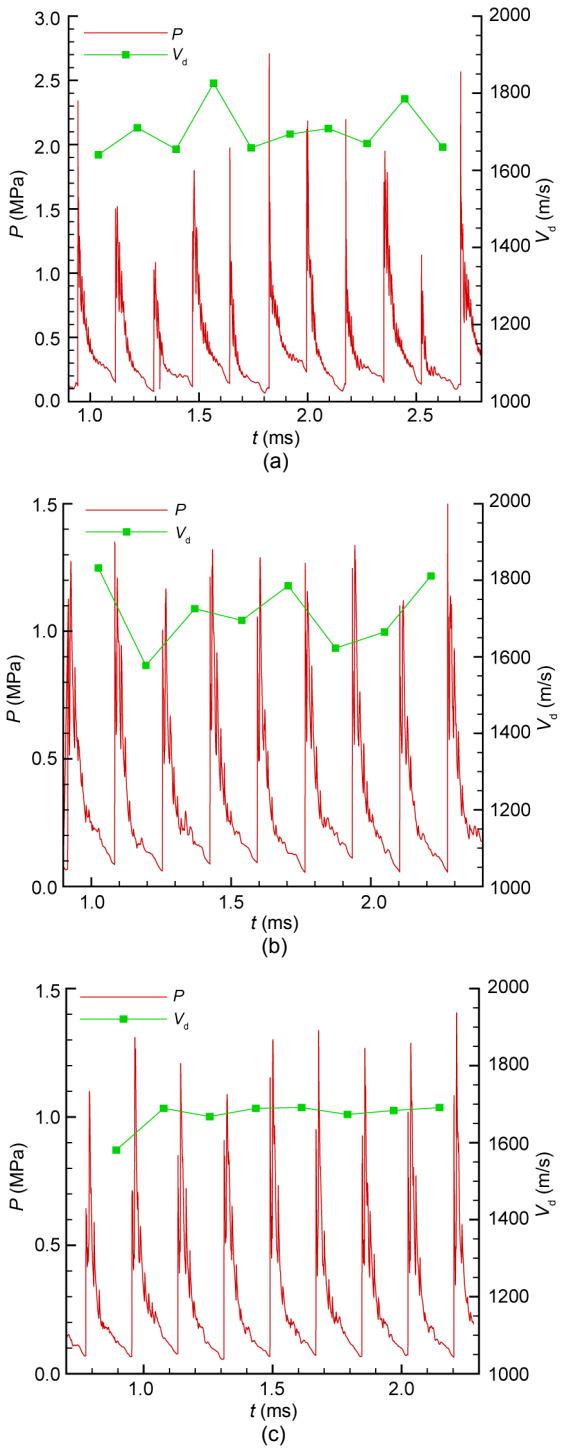

Fig. 8 Pressure record curves of P2 in the chamber
(a) Case A0; (b) Case A1; (c) Case A2

In order to investigate the flow fields in the plenum, pressure contours with the highest level of 0.8 MPa are shown in Fig. 9. From the snapshots, we can see that an upstream oblique wave is formed by the high pressure behind the CRD wave, and a reflected wave is generated after the oblique shock wave meets the inlet boundary. Obviously, peak pressures can be captured when the oblique shock wave passes the monitor point P1. The propagation frequency of the oblique wave in the plenum is almost the same as that of the CRD wave in the chamber. Fig. 10 shows the pressure record curves of P1 in the plenum. The peak pressures in the plenum decline from approximately 1.2 MPa to about 0.8 MPa as W increases from 6 mm to 10 mm. For quantitative study of the non-uniformity of pressure in the plenum, the average pressure in the plenum ($\overline{P}_{\text{plenum}}$) and the relative standard deviation of the pressure in the plenum (δ) are both analyzed, and are calculated with the values recorded by P1. In line with the trend of $\overline{V}_{\text{d}}$, δ decreases considerably as W increases in Fig. 11. The results listed in Table 4 show that δ reduces by 16.67% as W increases from 6 mm to 10 mm.

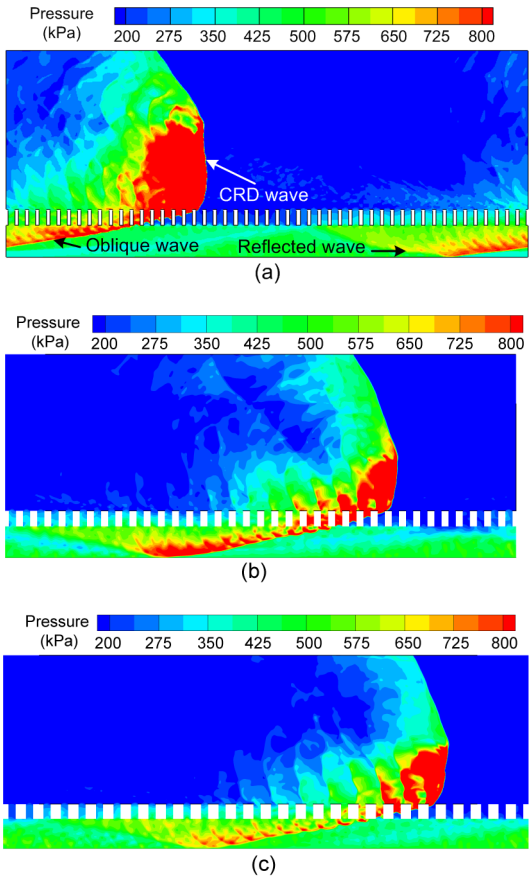

Fig. 9 Pressure contours of Cases A0–A2
(a) Case A0; (b) Case A1; (c) Case A2

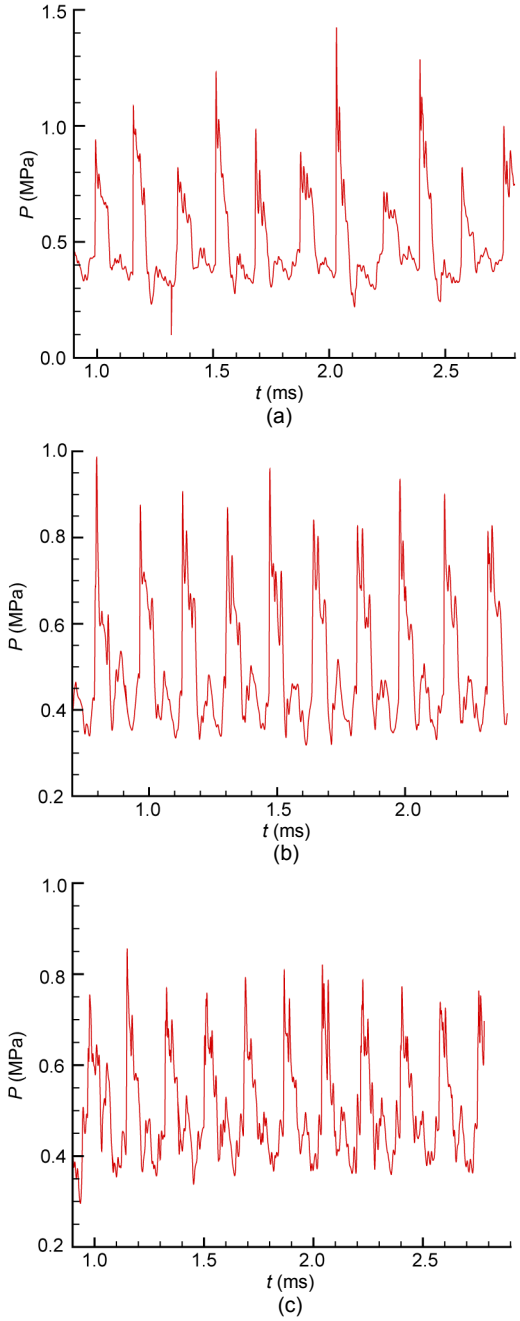

Fig. 10 Pressure record curves of P1 in the plenum
(a) Case A0; (b) Case A1; (c) Case A2

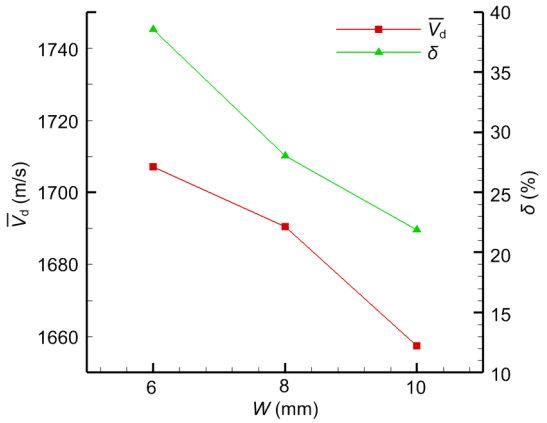

Fig. 11 $\overline{V}_d$ and δ vs. W

Table 4 Calculated results of the cases in this study

Case	$\overline{P}_{plenum}$ (Pa)	δ (%)	$\overline{V}_d$ (m/s)
A0	497 500.65	38.56	1707.09
A1	495 280.80	28.02	1690.45
A2	496 702.77	21.89	1657.38
B1	497 963.26	17.33	1650.79
B2	498 720.65	30.28	1695.08
C1	498 359.31	25.77	1792.28
C2	495 308.92	36.47	1521.99
C3	496 099.62	10.72	2021.02
C4	502 254.34	24.09	1351.63

3.2 Effects of the nozzle exit width

In this section, Cases B1, B2, and A0 with different nozzle exit widths W_e (2 mm, 3 mm, and 4 mm) are analyzed. As Fig. 12 illustrates, the structures of the flow fields show little difference. High-temperature strips also persist between the gaps. The CRD waves in these cases all propagate in single-wave mode during the whole operating time. $\overline{V}_d$ rises from 1650.79 m/s to 1707.09 m/s as W_e increases from 2 mm to 4 mm. According to the pressure curves obtained by P2 in Fig. 13, most peak pressures in the chamber of Case A0 are higher than those in the other two cases, in which most of the peak pressures are lower than 1.5 MPa. All these results indicate that larger W_e is conducive to forming a stronger CRD wave. On the other hand, as Fig. 14 shows, the pressure response in the plenum is much weaker in the case with smaller W_e. The peak pressure in the plenum is about 0.7 MPa in Case B1 whose W_e is the smallest at 2 mm. Sharing the same tendency with $\overline{V}_d$, δ increases moderately as W_e enlarges. As Fig. 15 shows, the value of δ goes up from 17.33% to 38.56% as W_e rises from 2 mm to 4 mm. The state of the plenum is more unstable when W_e gets larger. It can be concluded that as W_e increases, the strength of the CRD wave and the feedback pressure into the plenum increase.

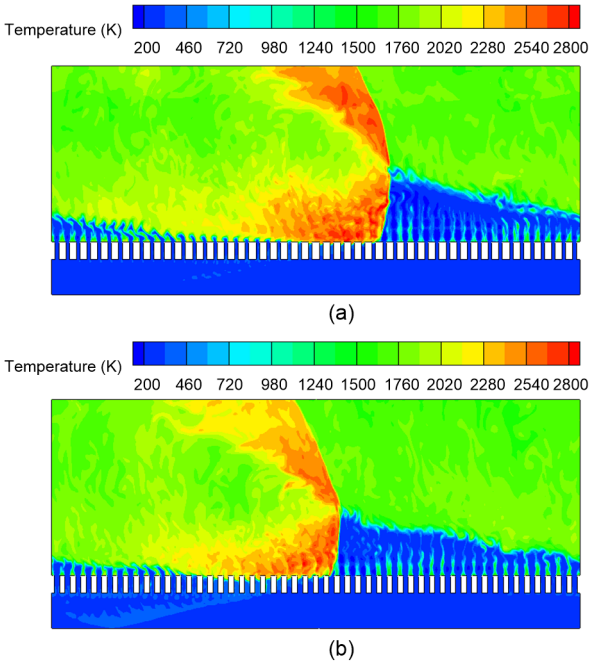

Fig. 12 Temperature contours of Case B1 and B2
(a) Case B1; (b) Case B2

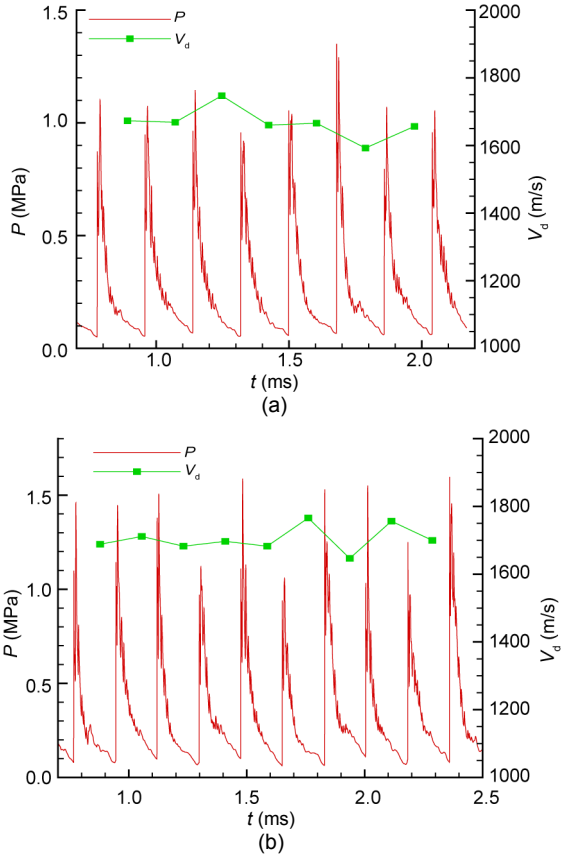

Fig. 13 Pressure record curves of P2 in the chamber
(a) Case B1; (b) Case B2

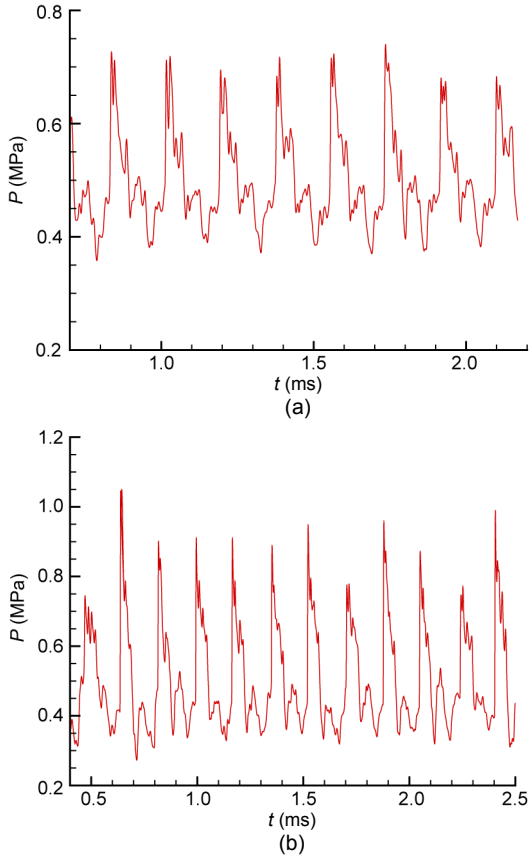

Fig. 14 Pressure record curves of P1 in the plenum
(a) Case B1; (b) Case B2

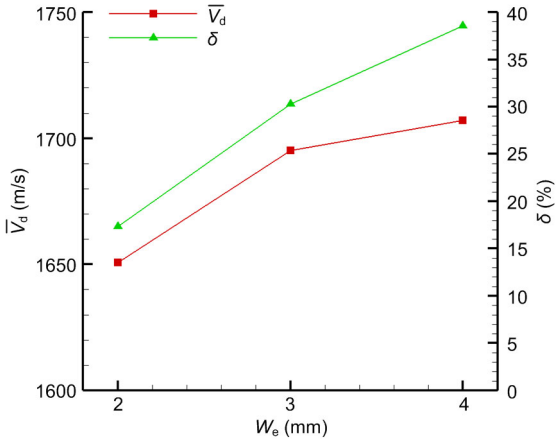

Fig. 15 $\overline{V}_d$ and δ vs. W_e

3.3 Effects of the slant angle of nozzle

In this section, Cases A0 and C1–C4 with different injection angles of 0°, 30°, −30°, 60°, and −60° are simulated. Cases C2 and C4 are ignited by the tangential flow with a high speed of −1200 m/s so that

the CRD wave propagates along the $-x$ direction. Thus, the nozzles slant against the propagation direction of the CRD wave and the slant angle of nozzle α is negative. According to the definition of α, a larger slant will be approached when the absolute value of α is higher.

Fig. 16 depicts the flow fields of cases with different α after the CRD wave reaches a stable propagation condition. The basic structures of the flow fields are similar except for some specific details. The CRD wave propagates in single-wave mode in most cases while the CRD waves propagate in a co-rotating two-wave mode in Case C1. The height of the CRD wave in Case A0 is the highest as the premixed gas is perpendicularly injected into the chamber establishing a high premixed gas layer in front of the wave. By contrast, the height of the CRD wave in Case C1 is the lowest due to less time for propellant injection and accumulation in the co-rotating two-wave mode. The fill regions in front of the CRD wave are also different. Due to the slight slant in Cases C1 and C2, the azimuthal velocity of fresh gas is not high enough to blow away the combustion products and so a few products persist between the gaps of injection nozzles. This may lead to parasitic combustion (a secondary combustion prior to the CRD wave is termed a parasitic combustion). Due to the larger slant in Cases C3 and C4, the premixed gas is obliquely injected into the chamber with higher azimuthal velocity, and few combustion products persist between the gaps making the premixed gas layer more uniform. Moreover, the top of the premixed gas layer in Case C3 curls up due to the high pressure behind the CRD wave.

The transition process is displayed in Fig. 17. At time t=0.46 ms, the fresh premixed gas is injected into the chamber and induced by the high-temperature combustion products in what is termed as parasitic combustion. Thus, a hotspot, named Hotspot1, is generated far behind the CRD wave named CRDW1. After its development, Hotspot1 gradually expands and moves forward consuming the fresh premixed gas. At time t=0.52 ms, the temperature of Hotspot1 rises to a high level, and another hotspot, named Hotspot2, is formed behind it. At the next moment, a new CRD wave named CRDW2 is formed because the reaction heat of Hotspot1 has been raised high enough by parasitic combustion. On the other hand, the strength of CRDW1 gets weaker as the height of the premixed gas layer before it is quite low. Hotspot2 fades away around time t=0.56 ms because there is not enough premixed gas in front of it. The new wave has fully developed at time t=0.58 ms and the CRD

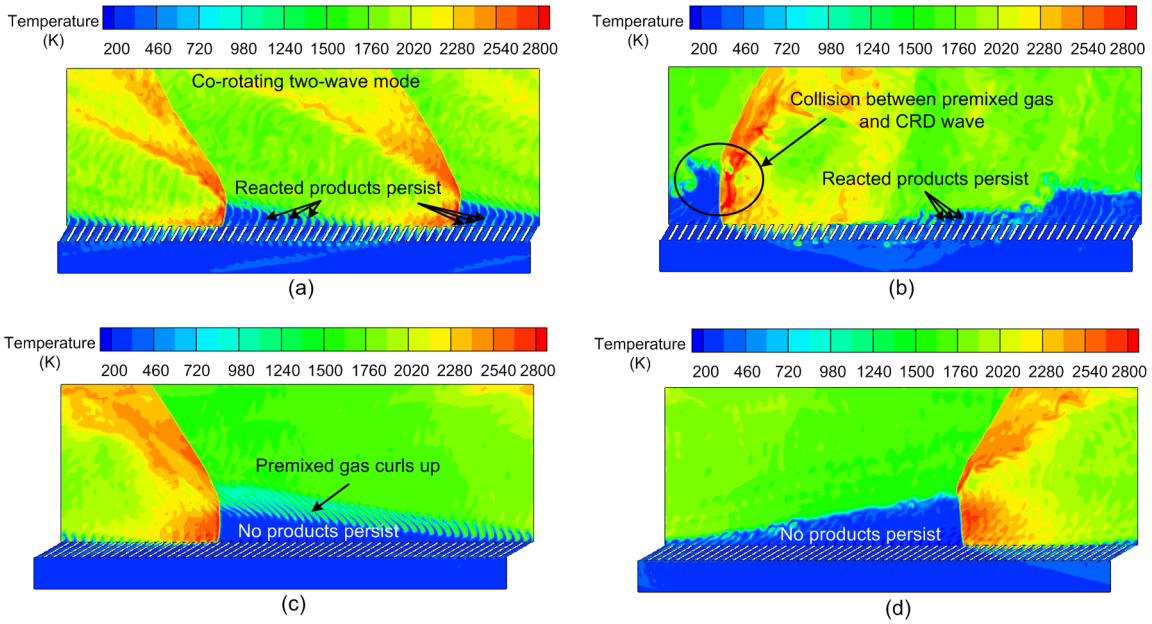

Fig. 16 Temperature contours of Cases C1–C4
(a) Case C1; (b) Case C2; (c) Case C3; (d) Case C4

waves will propagate steadily thereafter. Parasitic combustion in the premixed gas layer may induce a new detonation wave, but that is not found in Cases C2, C3, and C4. In Case C1, the azimuthal velocity of the fresh gas may help to develop the new wave. When the premixed gas is injected at a slant into the chamber in the propagation direction of the CRD wave, the fresh gas obtains an azimuthal velocity, which helps the hotspot to spread forward. Consequently, the hotspot is prevented from being overtaken and swallowed by the current CRD wave. This is the reason why there is only a CRD wave in Case A0 even if parasitic combustion exists.

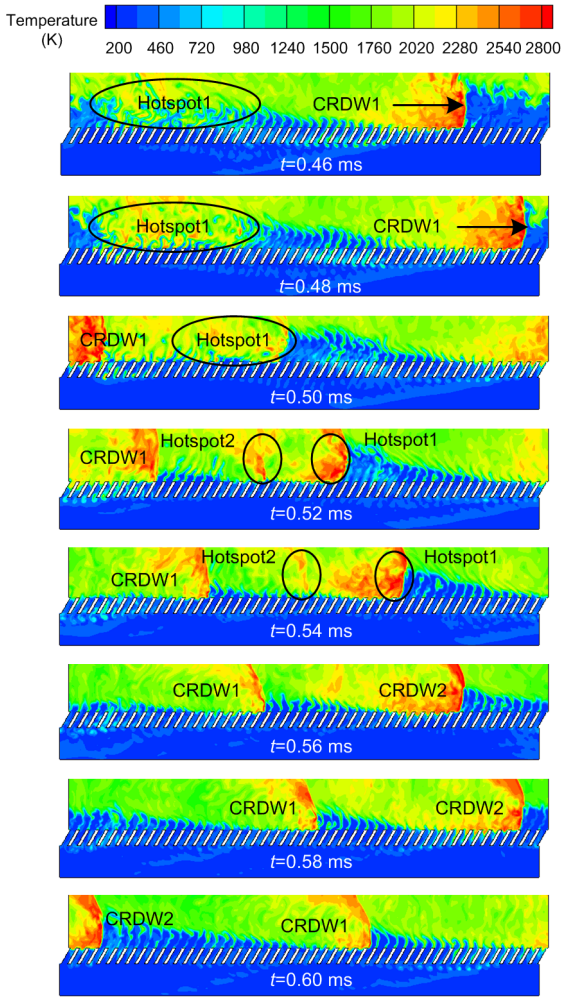

Fig. 17 Transition process from one-wave mode to two-wave mode in Case C1

Fig. 18 shows the pressure record curves obtained in the chamber. When the premixed gas is injected at a slant, we find the peak pressures in the chamber are much higher and more stable. Although the co-rotating two-wave mode is observed in Case C1, the peak pressures are still high. That indicates that the strength of the CRD wave is improved when the gas is injected at a slant. Since the azimuthal velocity of the fresh gas V_{gas} can be obtained, the relative CRD wave propagation velocity V_{d0} which is relative to the freshly injected gas can be calculated by $V_{d0}=\overline{V}_d-V_{gas}$. It is worth noting that V_{gas} is positive when the nozzles slant in the propagation direction of the CRD wave; otherwise, V_{gas} is negative. As listed in Table 5, V_{d0} fluctuates slightly in different cases. However, as Fig. 19 shows, the visible velocity of CRD wave $\overline{V}_d$ increases monotonically as α increases. The highest $\overline{V}_d$ is 2021.02 m/s achieved in Case C3 (α=60°). When α is negative, a great reduction in $\overline{V}_d$ is found and the lowest $\overline{V}_d$ is just 1351.63 m/s in Case C4 (α=−60°). The fresh gas with great azimuthal velocity in the propagation direction of the CRD wave helps to accelerate the propagation of the wave and this results in high $\overline{V}_d$ in both Cases C1 and C3. By contrast, when the fresh gas is injected on the slant against the propagation direction of the CRD wave, the collision (shown in Fig. 16c) between premixed gas and CRD wave significantly decelerates the propagation of the CRD wave. Above all, injecting premixed gas in the propagation direction of the CRD wave is conducive to improving the visible velocity of CRD wave.

Table 5 $\overline{V}_d$, V_{gas}, and V_{d0} of Cases A0 and C1–C4

Case	$\overline{V}_d$ (m/s)	V_{gas} (m/s)	V_{d0} (m/s)
A0	1707.09	4.15	1702.84
C1	1792.28	163.96	1628.32
C2	1521.99	−166.32	1688.31
C3	2021.02	333.87	1687.15
C4	1351.63	−336.36	1687.99

Fig. 20 (p.560) demonstrates the feedback pressure into the plenum. Peak pressures in the plenum are much lower when the propellant is injected into the chamber at a slant. Pressure response is slight

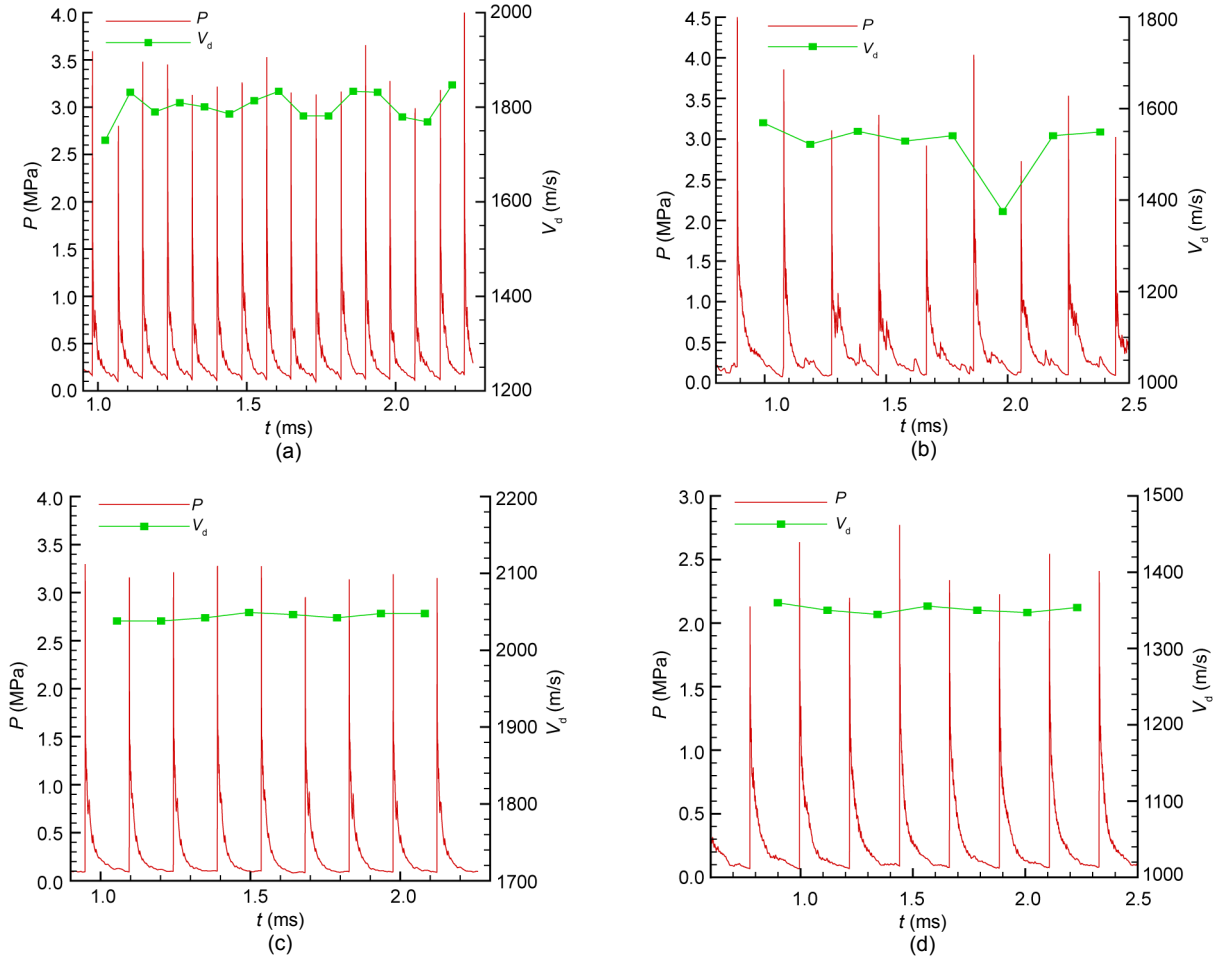

Fig. 18 Pressure record curves of P2 in the chamber
(a) Case C1; (b) Case C2; (c) Case C3; (d) Case C4

when the nozzle is highly slanted (α=±60°). The lowest feedback pressure is obtained in Case C3 where the peak pressures in the plenum are about 0.65 MPa. Lower feedback pressure is acquired when α is positive with the same absolute value. This means more significant inhibition of feedback pressure is acquired when nozzles slant in the propagation direction of the CRD wave. The calculated results of δ listed in Table 4 support this argument. In Cases C1 and C3 with positive α, δ is just 25.77% and 10.72% while it increases to 36.47% and 24.09% correspondingly in Cases C2 and C4 with negative α. As Fig. 19 shows, δ in Cases C1–C4 is lower than in Case A0, indicating that slant injection is helpful in achieving a more stable state in the plenum. The highest $\overline{V}_d$ and the lowest δ are both obtained when α=60° in Case C3. These results indicate that a large slant of the nozzles in the propagation direction of CRD wave is more beneficial for acquiring both a strong CRD wave and a stable state of the plenum.

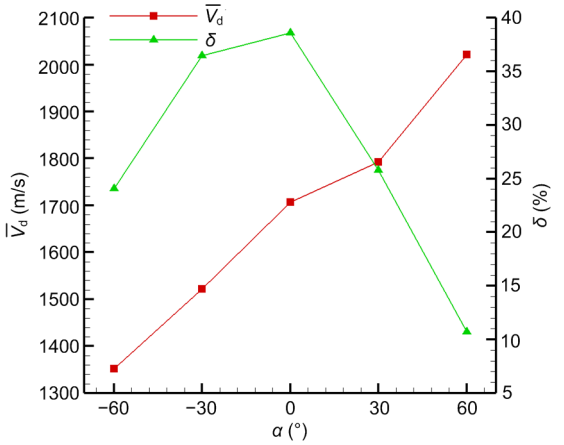

Fig. 19 $\overline{V}_d$ and δ vs. α

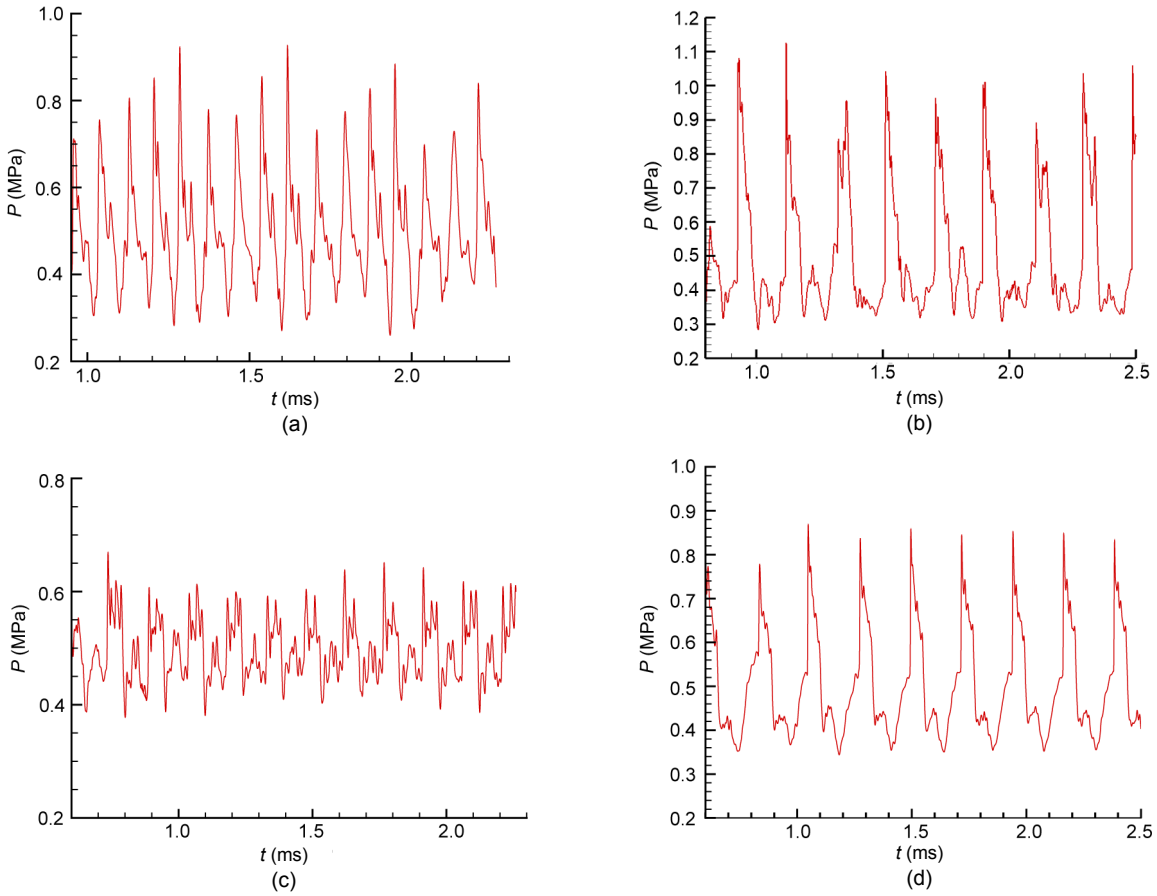

Fig. 20 Pressure record curves of P1 in the plenum
(a) Case C1; (b) Case C2; (c) Case C3; (d) Case C4

4 Conclusions

In order to investigate the effects of injection nozzle on ethylene-air CRDE, a series of simulations with different nozzles has been conducted and is described in this paper. Ethylene-air CRD waves are successfully established using nozzles of different geometrical parameters. Through the pressure record curves, temperature contours, and pressure contours, simulation results have been analyzed. The conclusions are as follows:

1. The distance between two neighboring nozzle centers has effects on both the CRD wave propagation and the feedback pressure into the plenum. Small W helps to improve the strength of the CRD wave and leads to great feedback pressure into the plenum. $\overline{V}_{\mathrm{d}}$ are estimated as 1707.09 m/s, 1690.45 m/s, and 1657.38 m/s when W are correspondingly 6 mm, 8 mm, and 10 mm. Meanwhile, peak pressures in the chamber in Case A0 can even exceed 2.5 MPa while most peak pressures of Cases A1 and A2 are lower than 1.5 MPa. Besides, the peak pressures in the plenum decline from approximately 1.2 MPa to about 0.8 MPa and δ reduces by 16.67% as W increases from 6 mm to 10 mm.

2. The intensity of the CRD wave is improved with the increase of nozzle exit width. As the strength of the CRD wave increases, the feedback pressure into the plenum increases. When W_{e} increases, more propellant will be injected into the chamber and the intensity of the CRD wave is improved. $\overline{V}_{\mathrm{d}}$ rises slightly from 1650.79 m/s to 1707.09 m/s as W_{e} increases from 2 mm to 4 mm. Most peak pressures in the chamber of Case A0 are higher than in the other two cases. On the other hand, low peak pressures in the plenum are obtained when W_{e}=2 mm. Moreover, the value of δ increases from 17.33% to 38.56% as W_{e} rises from 2 mm to 4 mm.

3. The slant angle of the nozzle has significant impact on the propagation velocity of the CRD wave and the feedback pressure into the plenum. When the nozzles slant in the propagation direction of the CRD wave, the visible velocity of CRD wave $\bar{V}_{\mathrm{d}}$ is greatly improved; otherwise, the velocity is greatly reduced. $\bar{V}_{\mathrm{d}}$ are 1707.09 m/s, 1792.28 m/s, and 2021.02 m/s when α are 0°, 30°, and 60°, respectively. However, $\bar{V}_{\mathrm{d}}$ declines to 1521.99 m/s and 1351.63 m/s when α are −30° and −60°, correspondingly. When the premixed gas is injected into the chamber at a slant, the feedback pressure into the plenum is inhibited. A greater slant is more likely to achieve a lower feedback pressure in the plenum. When α is 0°, δ is the highest reaching 38.56%. However, δ moderately decreases to 25.77% and 36.47% when α changes to 30° and −30° correspondingly. Furthermore, δ are just 10.72% and 24.09% when α are 60° and −60°, respectively. The highest $\bar{V}_{\mathrm{d}}$ and the lowest δ are both obtained when α=60°.

4. Injection with a slant angle can also change the propagation mode of the CRD wave. The co-rotating two-wave mode is observed when the premixed gas is injected on a slant into the chamber in Case C1. The parasitic combustion induces a hotspot, and the azimuthal velocity of the premixed gas in the propagation direction of the CRD wave contributes to the formation of a new CRD wave.

This paper provides deeper understanding of the ethylene-air CRD wave and enriches the nozzle design theory for CRDE. Some further research on this topic considering mixing efficiency should be conducted in the near future.

Contributors

Jin ZHOU and Shi-jie LIU participated in the design of this numerical study. Wei-jie FAN carried out the simulations and analyzed the results under their guidance. Hao-yang PENG provided important suggestions on the improvement of simulation. All authors reviewed and revised the manuscript carefully, and approved the content of the manuscript.

Conflict of interest

Wei-jie FAN, Jin ZHOU, Shi-jie LIU, and Hao-yang PENG declare that they have no conflict of interest.

References

Anand V, George ACS, Driscoll RB, et al., 2015. Statistical treatment of wave instability in rotating detonation combustors. Proceedings of the 53rd AIAA Aerospace Sciences Meeting. https://doi.org/10.2514/6.2015-1103

Anand V, George AS, Driscoll R, et al., 2016a. Analysis of air inlet and fuel plenum behavior in a rotating detonation combustor. *Experimental Thermal and Fluid Science*, 70:408-416. https://doi.org/10.1016/j.expthermflusci.2015.10.007

Anand V, George AS, Driscoll R, et al., 2016b. Investigation of rotating detonation combustor operation with H_2-air mixtures. *International Journal of Hydrogen Energy*, 41(2):1281-1292. https://doi.org/10.1016/j.ijhydene.2015.11.041

Bykovskii FA, Vedernikov EF, 1996. Self-sustaining pulsating detonation of gas-mixture flow. *Combustion, Explosion and Shock Waves*, 32(4):442-448. https://doi.org/10.1007/BF01998496

Cai XD, Liang JH, Deiterding R, et al., 2016. Adaptive mesh refinement based simulations of three-dimensional detonation combustion in supersonic combustible mixtures with a detailed reaction model. *International Journal of Hydrogen Energy*, 41(4):3222-3239. https://doi.org/10.1016/j.ijhydene.2015.11.093

Davidenko DM, Gökalp I, Kudryavtsev AN, 2007. Numerical simulation of the continuous rotating hydrogen-oxygen detonation with a detailed chemical mechanism. West-east High Speed Flow Field Conference, p.19-22.

Driscoll R, George AS, Gutmark EJ, 2016. Numerical investigation of injection within an axisymmetric rotating detonation engine. *International Journal of Hydrogen Energy*, 41(3):2052-2063. https://doi.org/10.1016/j.ijhydene.2015.10.055

Frolov SM, Dubrovskii AV, Ivanov VS, et al., 2013. Three-dimensional numerical simulation of the operation of a rotating-detonation chamber with separate supply of fuel and oxidizer. *Russian Journal of Physical Chemistry B*, 7(1):35-43. https://doi.org/10.1134/S1990793113010119

Fujii J, Kumazawa Y, Matsuo A, et al., 2016. Numerical investigation on detonation velocity in rotating detonation engine chamber. *Proceedings of the Combustion Institute*, 36(2):2665-2672. https://doi.org/10.1016/j.proci.2016.06.155

Gaillard T, Davidenko D, Dupoirieux F, 2017. Numerical simulation of a rotating detonation with a realistic injector designed for separate supply of gaseous hydrogen and oxygen. *Acta Astronautica*, 141:64-78. https://doi.org/10.1016/j.actaastro.2017.09.011

Hishida M, Fujiwara T, Wolanski P, 2009. Fundamentals of rotating detonations. *Shock Waves*, 19(1):1-10. https://doi.org/10.1007/s00193-008-0178-2

Huang SY, Zhou J, Liu SJ, et al., 2019. Effects of pintle injector on ethylene-air rocket-based continuous rotating detonation. *Acta Astronautica*, 164:311-320. https://doi.org/10.1016/j.actaastro.2019.08.019

Huang W, Chang JT, Yan L, 2020. Mixing and combustion

in supersonic/hypersonic flows. *Journal of Zhejiang University-SCIENCE A (Applied Physics & Engineering)*, 21(8):609-613. https://doi.org/10.1631/jzus.A20MCSF1

Kindracki J, Wolański P, Gut Z, et al., 2011. Experimental research on the rotating detonation in gaseous fuels–oxygen mixtures. *Shock Waves*, 21(2):75-84. https://doi.org/10.1007/s00193-011-0298-y

Lei ZD, Chen ZW, Yang XQ, et al., 2020a. Operational mode transition in a rotating detonation engine. *Journal of Zhejiang University-SCIENCE A (Applied Physics & Engineering)*, 21(9):721-733. https://doi.org/10.1631/jzus.A1900349

Lei ZD, Yang XQ, Ding J, et al., 2020b. Performance of rotating detonation engine with stratified injection. *Journal of Zhejiang University-SCIENCE A (Applied Physics & Engineering)*, 21(9):734-744. https://doi.org/10.1631/jzus.A1900383

Li BX, Wu YW, Weng CS, et al., 2018. Influence of equivalence ratio on the propagation characteristics of rotating detonation wave. *Experimental Thermal and Fluid Science*, 93:366-378. https://doi.org/10.1016/j.expthermflusci.2018.01.014

Lin W, Zhou J, Liu SJ, et al., 2015. Experimental study on propagation mode of H_2/air continuously rotating detonation wave. *International Journal of Hydrogen Energy*, 40(4):1980-1993. https://doi.org/10.1016/j.ijhydene.2014.11.119

Liu M, Zhou R, Wang JP, 2015. Numerical investigation of different injection patterns in rotating detonation engines. *Combustion Science and Technology*, 187(3):343-361. https://doi.org/10.1080/00102202.2014.923411

Liu SJ, Lin ZY, Sun MB, et al., 2011. Thrust vectoring of a continuous rotating detonation engine by changing the local injection pressure. *Chinese Physics Letters*, 28(9): 094704. https://doi.org/10.1088/0256-307X/28/9/094704

Liu SJ, Peng HY, Liu WD, et al., 2020. Effects of cavity depth on the ethylene-air continuous rotating detonation. *Acta Astronautica*, 166:1-10. https://doi.org/10.1016/j.actaastro.2019.09.038

Liu YS, Wang YH, Li YS, et al., 2015. Spectral analysis and self-adjusting mechanism for oscillation phenomenon in hydrogen-oxygen continuously rotating detonation engine. *Chinese Journal of Aeronautics*, 28(3):669-675. https://doi.org/10.1016/j.cja.2015.03.006

Meng QY, Zhao NB, Zheng HT, et al., 2018. Numerical investigation of the effect of inlet mass flow rates on H_2/air non-premixed rotating detonation wave. *International Journal of Hydrogen Energy*, 43(29):13618-13631. https://doi.org/10.1016/j.ijhydene.2018.05.115

Morris C, 2005. Axisymmetric modeling of pulse detonation rocket engines. Proceedings of the 41st AIAA/ASME/SAE/ASEE Joint Propulsion Conference & Exhibit. https://doi.org/10.2514/6.2005-3508

Naples A, Hoke J, Schauer F, 2015. Experimental investigation of a rotating detonation engine injector temporal response. Proceedings of the 53rd AIAA Aerospace Sciences Meeting. https://doi.org/10.2514/6.2015-1104

Nicholls JA, Cullen RE, Ragland KW, 1966. Feasibility studies of a rotating detonation wave rocket motor. *Journal of Spacecraft and Rockets*, 3(6):893-898. https://doi.org/10.2514/3.28557

Nikitin VF, Dushin VR, Phylippov YG, et al., 2009. Pulse detonation engines: technical approaches. *Acta Astronautica*, 64(2-3):281-287. https://doi.org/10.1016/j.actaastro.2008.08.002

Nordeen CA, Schwer D, Schauer F, et al., 2016. Role of inlet reactant mixedness on the thermodynamic performance of a rotating detonation engine. *Shock Waves*, 26(4):417-428.

Peng HY, Liu WD, Liu SJ, et al., 2019a. The effect of cavity on ethylene-air continuous rotating detonation in the annular combustor. *International Journal of Hydrogen Energy*, 44(26):14032-14043. https://doi.org/10.1016/j.ijhydene.2019.04.017

Peng HY, Liu WD, Liu SJ, et al., 2019b. Realization of methane-air continuous rotating detonation wave. *Acta Astronautica*, 164:1-8. https://doi.org/10.1016/j.actaastro.2019.07.001

Rankin BA, Fotia M, Paxson DE, et al., 2015. Experimental and numerical evaluation of pressure gain combustion in a rotating detonation engine. Proceedings of the 53rd AIAA Aerospace Sciences Meeting. https://doi.org/10.2514/6.2015-0877

Schwer D, Kailasanath K, 2011. Numerical study of the effects of engine size on rotating detonation engines. Proceedings of the 49th AIAA Aerospace Sciences Meeting Including the New Horizons Forum and Aerospace Exposition. https://doi.org/10.2514/6.2011-581

Schwer D, Kailasanath K, 2012. Feedback into mixture plenums in rotating detonation engines. Proceedings of the 50th AIAA Aerospace Sciences Meeting Including the New Horizons Forum and Aerospace Exposition. https://doi.org/10.2514/6.2012-617

Schwer D, Kailasanath K, 2013. Fluid dynamics of rotating detonation engines with hydrogen and hydrocarbon fuels. *Proceedings of the Combustion Institute*, 34(2):1991-1998. https://doi.org/10.1016/j.proci.2012.05.046

Schwer D, Corrigan A, Taylor B, et al., 2013. On reducing feedback pressure in rotating detonation engines. Proceedings of the 51st AIAA Aerospace Sciences Meeting Including the New Horizons Forum and Aerospace Exposition. https://doi.org/10.2514/6.2013-1178

Shao YT, Liu M, Wang JP, et al., 2010. Numerical investigation of rotating detonation engine propulsive performance. *Combustion Science and Technology*, 182(11-12): 1586-1597.

https://doi.org/10.1080/00102202.2010.497316

Shi W, Tian Y, Zhang WZ, et al., 2020. Experimental investigation on flame stabilization of a kerosene-fueled scramjet combustor with pilot hydrogen. *Journal of Zhejiang University-SCIENCE A (Applied Physics & Engineering)*, 21(8):663-672. https://doi.org/10.1631/jzus.A1900565

Singh DJ, Jachimowski CJ, 1994. Quasiglobal reaction model for ethylene combustion. *AIAA Journal*, 32(1):213-216. https://doi.org/10.2514/3.11972

Smirnov NN, Betelin VB, Nikitin VF, et al., 2015. Accumulation of errors in numerical simulations of chemically reacting gas dynamics. *Acta Astronautica*, 117:338-355. https://doi.org/10.1016/j.actaastro.2015.08.013

Smirnov NN, Nikitin VF, Stamov LI, et al., 2018. Rotating detonation in a ramjet engine three-dimensional modeling. *Aerospace Science and Technology*, 81:213-224. https://doi.org/10.1016/j.ast.2018.08.003

Stewart DS, Kasimov AR, 2006. State of detonation stability theory and its application to propulsion. *Journal of Propulsion and Power*, 22(6):1230-1244. https://doi.org/10.2514/1.21586

Sun J, Zhou J, Liu SJ, et al., 2017. Effects of injection nozzle exit width on rotating detonation engine. *Acta Astronautica*, 140:388-401. https://doi.org/10.1016/j.actaastro.2017.09.008

Sun J, Zhou J, Liu SJ, et al., 2018a. Numerical investigation of a rotating detonation engine under premixed/non-premixed conditions. *Acta Astronautica*, 152:630-638. https://doi.org/10.1016/j.actaastro.2018.09.012

Sun J, Zhou J, Liu SJ, et al., 2018b. Plume flowfield and propulsive performance analysis of a rotating detonation engine. *Aerospace Science and Technology*, 81:383-393. https://doi.org/10.1016/j.ast.2018.08.024

Sun J, Zhou J, Liu SJ, et al., 2019. Effects of air injection throat width on a non-premixed rotating detonation engine. *Acta Astronautica*, 159:189-198. https://doi.org/10.1016/j.actaastro.2019.03.067

Sun YC, Cai Z, Wang TY, et al., 2020. Numerical study on cavity ignition process in a supersonic combustor. *Journal of Zhejiang University-SCIENCE A (Applied Physics & Engineering)*, 21(10):848-858. https://doi.org/10.1631/jzus.A1900419

Taki S, Fujiwara T, 1978. Numerical analysis of two-dimensional nonsteady detonations. *AIAA Journal*, 16(1):73-77. https://doi.org/10.2514/3.60859

Voitsekhovskii BV, 1959. Stationary spin detonation. *Doklady Akademii Nayk USSR*, 129(6):1254-1256.

Wang P, Shen CB, 2019. Characteristics of mixing enhancement achieved using a pulsed plasma synthetic jet in a supersonic flow. *Journal of Zhejiang University-SCIENCE A (Applied Physics & Engineering)*, 20(9):701-713. https://doi.org/10.1631/jzus.A1900130

Wang YH, Le JL, Wang C, et al., 2018. A non-premixed rotating detonation engine using ethylene and air. *Applied Thermal Engineering*, 137:749-757. https://doi.org/10.1016/j.applthermaleng.2018.04.015

Xie QF, Wen HC, Li WH, et al., 2018. Analysis of operating diagram for H_2/air rotating detonation combustors under lean fuel condition. *Energy*, 151:408-419. https://doi.org/10.1016/j.energy.2018.03.062

Yao S, Han X, Liu Y, et al., 2017. Numerical study of rotating detonation engine with an array of injection holes. *Shock Waves*, 27(3):467-476. https://doi.org/10.1007/s00193-016-0692-6

Zhdan SA, 2008. Mathematical model of continuous detonation in an annular combustor with a supersonic flow velocity. *Combustion, Explosion, and Shock Waves*, 44(6):690-697. https://doi.org/10.1007/s10573-008-0104-z

Zhdan SA, Mardashev AM, Mitrofanov VV, 1990. Calculation of the flow of spin detonation in an annular chamber. *Combustion, Explosion and Shock Waves*, 26(2):210-214. https://doi.org/10.1007/BF00742414

Zhdan SA, Bykovskii FA, Vedernikov EF, 2007. Mathematical modeling of a rotating detonation wave in a hydrogen-oxygen mixture. *Combustion, Explosion, and Shock Waves*, 43(4):449-459. https://doi.org/10.1007/s10573-007-0061-y